European Radiology

Hypoxia and perfusion in breast cancer: simultaneous assessment using PET/MR imaging

--Manuscript Draft--

Manuscript Number:	EURA-D-20-00620R1
Full Title:	Hypoxia and perfusion in breast cancer: simultaneous assessment using PET/MR imaging
Article Type:	Original Article
Funding Information:	Cancer Research UK - Cambridge Institute (CCCIT-02) — Prof Fiona J Gilbert National Institute for Health Research (NIHR) - Cambridge Biomedical Research Centre — Prof Fiona J Gilbert
Abstract:	Objectives: Hypoxia is associated with poor prognosis and treatment resistance in breast cancer. However, the temporally-variant nature of hypoxia can complicate interpretation of imaging findings. We explored the relationship between hypoxia and vascular function in breast tumours through combined 18F-fluoromisonidazole (18F-FMISO) PET/MRI, with simultaneous assessment circumventing the effect of temporal variation in hypoxia and perfusion. Methods: Women with histologically-confirmed, primary breast cancer underwent a simultaneous 18 F-FMISO PET/MR examination. Tumour hypoxia was assessed using influx rate-constant Ki and hypoxic fractions (%HF), while parameters of vascular function (Ktrans, kep, ve, vp) and cellularity (ADC) were derived from DCE and DW-MRI, respectively. Additional correlates included histological subtype, grade and size. Relationships between imaging variables were assessed using Pearson correlation (r). Results: Twenty-nine women with 32 lesions were assessed. Hypoxic fractions >1% were observed in 6/32 (19%) cancers, while 18/32 (56%) tumours showed a %HF of zero. The presence of hypoxia in lesions was independent of histological subtype or grade. Mean tumour Ktrans correlated negatively with Ki (r=-0.38, p=0.04) and %HF (r=-0.33, p=0.04), though parametric maps exhibited intra-tumoral heterogeneity with hypoxic regions colocalising with both hypo and hyperperfused areas. No correlation was observed between ADC and DCE-MRI or PET parameters. %HF correlated positively with lesion size (r=0.63, p=0.001). Conclusion: Hypoxia measured by 18F-FMISO-PET correlated negatively with Ktrans from DCE-MRI supporting the hypothesis of perfusion-driven hypoxia in breast cancer. Intratumoural hypoxia-perfusion relationships were heterogeneous, suggesting that combined assessment may be needed for disease characterisation, which could be achieved using simultaneous multi-modality imaging.
Corresponding Author:	Fiona Gilbert University of Cambridge, Department of Radiology, BOX 218, Level 5, Addenbrooke's Hospital, Hills Road, Cambridge, UNITED KINGDOM
Corresponding Author Secondary Information:	
Corresponding Author's Institution:	University of Cambridge, Department of Radiology, BOX 218, Level 5, Addenbrooke's Hospital, Hills Road,
Corresponding Author's Secondary Institution:	
First Author:	Julia C Carmona-Bozo, MD
First Author Secondary Information:	
Order of Authors:	Julia C Carmona-Bozo, MD
	Roido Manavaki, PhD
	Ramona Woitek, MD, PhD

	Turid Torheim, PhD
	Gabrielle C Baxter, MPhys
	Corradina Caracò, MD
	Elena Provenzano, MD
	Martin J Graves, PhD
	Tim D Fryer, PhD
	Andrew J Patterson, PhD
	Fiona J Gilbert, MD
Order of Authors Secondary Information:	
Author Comments:	Fiona J. Gilbert, FRCR, FRCP Professor of Radiology Head of Department Department of Radiology School of Clinical Medicine University of Cambridge Box 218 | Cambridge Biomedical Campus Cambridge, UK CB2 0QQ Professor Yves Menu, Editor-in-Chief European Radiology 19th February 2020 Dear Professor Menu, We would be grateful if the enclosed manuscript entitled “Hypoxia and perfusion in breast cancer: Simultaneous assessment using PET/MR imaging” could be considered for publication in European Radiology. The manuscript is an original research report exploring the relationship between hypoxia and parameters of perfusion and vascular permeability in breast cancer using simultaneous positron emission tomography/magnetic resonance imaging (PET/MRI), with 18F-fluoromisonidazole (18F-FMISO) used to assess hypoxia. There is ample evidence in the oncology literature about the importance of a hypoxic tumour microenvironment as a risk factor for treatment resistance and metastasis in breast cancer. However, even though hypoxia has been recognised as a significant indicator of poor clinical outcome, the reproducibility of in vivo imaging descriptors of hypoxia and other aspects of the tumour micro-environment, such as perfusion, as well as the correlations between them, have been inconsistent. Partially, the observed discrepancies may be due to imaging not always being able to macroscopically capture pathophysiologic processes observed at the microscale. However, temporal variance in processes like hypoxia and perfusion is also thought to have an important impact on the results. In this study, in order to remove the confounding effect of temporal variance in hypoxia and perfusion, we performed simultaneous PET/MR imaging. Aside from the logistical and methodological advantages that combined PET/MR acquisition can offer, such as improved spatial registration between hypoxia and perfusion parameters from PET and MRI respectively, it also allows imaging of tumours under the same physiologic conditions, achieving physiological simultaneity within the imaging time frame. To our knowledge, this is the first study in breast cancer attempting to simultaneously explore associations between hypoxia and perfusion via in vivo imaging. In the sample of breast cancers examined (n=32), we found an inverse relationship between tumour hypoxia measured by 18F-FMISO-PET and perfusion measured by dynamic contrast-enhanced (DCE) MRI, which was independent of tumour histology or

grade. Hypoxic fractions in tumours demonstrated an increase with tumour size. Significant intra-tumoral heterogeneity was observed in hypoxia-perfusion patterns, which is indicative of the hypoxic variability encountered in breast cancer and in line with recently published literature (Bandhari et al. Nat Genet. 51:308-18, 2019).

We feel that these findings would be of interest in the following respect. Though the perfusion-related increase in hypoxia at the tumour level would suggest that perfusion could potentially act as a surrogate marker of hypoxia in breast cancer, the intra-tumoral heterogeneity in hypoxia-perfusion patterns illustrates the potential role of simultaneous multi-modality imaging in characterising disease and understanding treatment efficacy in breast cancer.

Preliminary results from this research have been presented in abstract form at the Annual Scientific Meeting of the British Society of Breast Radiology (BSBR), Dublin, Ireland, 2017 [Carmona-Bozo et al. Hypoxia in ER+ breast cancer: a study using combined PET/MR imaging. Breast Cancer Res 19:116, 2017 (suppl; abstr PB.10)], and the European Congress of Radiology (ECR), Vienna, Austria, 2018 [Carmona-Bozo J et al. Imaging of the hypoxic microenvironment in breast cancer using PET/MR].

This study was co-funded by Cancer Research UK (CRUK) – Cambridge Institute (CCCIT02) and National Institute for Health Research (NIHR) Cambridge Biomedical Research Centre (BRC).

The work described in the manuscript is entirely our own and is not being considered for publication elsewhere. All authors listed on the manuscript have made substantial contributions to the concept or design of the work, or the acquisition, analysis, or interpretation of data; have drafted or critically revised and approved the attached version of the manuscript.

Yours sincerely,

Fiona Gilbert

Title: Hypoxia and perfusion in breast cancer: simultaneous assessment using PET/MR imaging

Authors: Julia C Carmona-Bozo[1], Roido Manavaki[1], Ramona Woitek[1,2], Turid Torheim[3], Gabrielle C Baxter[1], Corradina Caracò[1], Elena Provenzano[3,4], Martin J Graves[1,5], Tim D Fryer[6], Andrew J Patterson[1,5], Fiona J Gilbert[1]

Affiliations

[1] Department of Radiology, School of Clinical Medicine, University of Cambridge, Box 218 – Cambridge Biomedical Campus, Cambridge, CB2 0QQ, UK.

[2] Department of Biomedical Imaging and Image-guided Therapy, Medical University of Vienna, Währinger Gürtel 18-20, 1090 Vienna, Austria.

[3] Cancer Research UK – Cambridge Institute, University of Cambridge, Li Ka Shing Centre, Robinson Way, Cambridge, CB2 0RE, UK.

[4] Cambridge Breast Unit, Cambridge University Hospitals NHS Foundation Trust, Box 97 – Cambridge Biomedical Campus Cambridge, CB2 0QQ, UK.

[5] MRIS Unit, Cambridge University Hospitals NHS Foundation Trust, Cambridge, Box 162 – Cambridge Biomedical Campus, Cambridge, CB2 0QQ, UK.

[6] Wolfson Brain Imaging Centre, Department of Clinical Neurosciences, School of Clinical Medicine, University of Cambridge, Box 65 – Cambridge Biomedical Campus, Cambridge, CB2 0QQ, UK.

Corresponding Author: Professor Fiona J Gilbert

Department of Radiology, School of Clinical Medicine, University of Cambridge, Box 218 – Cambridge Biomedical Campus, Cambridge, CB2 0QQ, UK

email: fjg28@medschl.cam.ac.uk

phone: (+)44 (0)1223 746439

Manuscript type: Original article

Title: Hypoxia and perfusion in breast cancer: simultaneous assessment using PET/MR imaging

Abstract

Objectives: Hypoxia is associated with poor prognosis and treatment resistance in breast cancer. However, the temporally-variant nature of hypoxia can complicate interpretation of imaging findings. We explored the relationship between hypoxia and vascular function in breast tumours through combined ^{18}F-fluoromisonidazole (^{18}F-FMISO) PET/MRI, with simultaneous assessment circumventing the effect of temporal variation in hypoxia and perfusion.

Methods: Women with histologically-confirmed, primary breast cancer underwent a simultaneous ^{18}F-FMISO PET/MR examination. Tumour hypoxia was assessed using influx rate-constant K_i and hypoxic fractions (%HF), while parameters of vascular function (K^{trans}, k_{ep}, v_e, v_p) and cellularity (ADC) were derived from DCE and DW-MRI, respectively. Additional correlates included histological subtype, grade and size. Relationships between imaging variables were assessed using Pearson correlation (r).

Results: Twenty-nine women with 32 lesions were assessed. Hypoxic fractions >1% were observed in 6/32 (19%) cancers, while 18/32 (56%) tumours showed a %HF of zero. The presence of hypoxia in lesions was independent of histological subtype or grade. Mean tumour K^{trans} correlated negatively with K_i (r=-0.38, p=0.04) and %HF (r=-0.33, p=0.04), though parametric maps exhibited intra-tumoral heterogeneity with hypoxic regions colocalising with both hypo and hyperperfused areas. No correlation was observed between ADC and DCE-MRI or PET parameters. %HF correlated positively with lesion size (r=0.63, p=0.001).

Conclusion: Hypoxia measured by ^{18}F-FMISO-PET correlated negatively with K^{trans} from DCE-MRI supporting the hypothesis of perfusion-driven hypoxia in breast cancer. Intratumoural hypoxia-perfusion relationships were heterogeneous, suggesting that combined assessment may be needed for disease characterisation, which could be achieved using simultaneous multi-modality imaging.

Keywords: PET/MRI, hypoxia, perfusion, breast cancer

Key points

- At the tumour level, hypoxia measured by ^{18}F-FMISO-PET, was negatively correlated with perfusion measured by DCE-MRI, which supports the hypothesis of perfusion-driven hypoxia in breast cancer.
- No associations were observed between ^{18}F-FMISO-PET parameters and tumour histology or grade, but tumour hypoxic-fractions increased with lesion size.
- Intra-tumoural hypoxia-perfusion relationships were heterogeneous, suggesting that the combined hypoxia-perfusion status of tumours may need to be considered for disease characterisation, which can be achieved via simultaneous multi-modality imaging as reported here.

Abbreviations: ^{18}F-FMISO: ^{18}F-fluoromisonidazole; K^{trans}: contrast influx transfer rate constant (mL/g/min); k_{ep}: contrast efflux rate constant (min^{-1}); v_e: extravascular-extracellular volume fraction; v_p: plasma volume fraction; K_i: tracer influx rate constant (mL/cm^3/min); %HF: percentage hypoxic fraction; SUV: standardised uptake value (g/mL); T_{max}/M: maximum tumour-to-muscle ratio; T_{max}/P: maximum tumour-to-plasma ratio; ADC: apparent diffusion coefficient (mm^2/s)

Introduction

Hypoxia is a common characteristic of the tumour microenvironment and arises due to avid metabolism and poor perfusion as a result of the structurally and functionally aberrant microcirculation found in tumours [1]. In breast cancer, the presence of hypoxia has been confirmed with pO_2 histography and occurs irrespective of histological type, molecular subtype, grade or patient characteristics [2,3]. *In vitro* studies have shown that hypoxia promotes a dedifferentiated phenotype in ductal carcinoma *in situ* [4] and downregulates the expression and function of oestrogen receptor-α (ERα) [5]. Several clinical and preclinical studies in breast cancer have demonstrated that overexpression of hypoxia-related proteins is associated with an aggressive phenotype, poor prognosis, and resistance to treatment [6-8].

Although tumour hypoxia can be broadly categorised as diffusion or perfusion-limited, it is generally accepted that the tumour microenvironment is a highly dynamic entity, exhibiting temporally-varying perfusion patterns and heterogeneous oxygen-tension gradients [9]. Experimental evidence suggests that oxygen levels continually fluctuate owing to transient changes in perfusion [10]. These changing perfusion and oxygenation levels induce a variety of gene expression profiles resulting in a unique micromilieu that is pivotal for tumour growth and metastatic dissemination [11]. Given the temporal variation in oxygenation and perfusion within tumours, sequential multi-modal imaging investigations may not always be effective in assessing the association between these parameters, as similar tumour status cannot be guaranteed between imaging sessions. Simultaneous assessment of the hypoxia and perfusion in tumours can mitigate confounders associated with the dynamic character of these processes, and thus allow additional pathophysiological characterisation of breast cancer.

Imaging methods, including positron emission tomography (PET) and magnetic resonance imaging (MRI), have been used for the non-invasive assessment of the tumour microenvironment. Dynamic contrast-enhanced (DCE) MRI has shown utility in characterising tumour perfusion and vascular permeability in clinical studies [12], while diffusion-weighted imaging (DWI) can provide surrogate measures of tumour cellular density [13]. PET with ^{18}F-labelled nitroimidazoles can provide specific measures of intracellular hypoxia [14]. In breast cancer, ^{18}F-fluoromisonidazole (^{18}F-FMISO) has been used for the evaluation of response to anti-angiogenic and HER2-targetted treatment [15,16] and shown potential utility as a predictor of response to primary endocrine therapy [17,18]. Additionally, high ^{18}F-FMISO uptake at

baseline has been associated with shorter disease-free survival [18] and disease-specific death [19].

Despite the intrinsic link between tumour hypoxia and perfusion, multi-modal imaging approaches to characterise this aspect of cancer pathophysiology have been limited in the clinical setting [16,19-24]. To effectively assess relationships between temporally-varying microenvironment parameters, combined PET/MR imaging presents an attractive option as it permits examination of the tumour under the same physiologic conditions, while also conferring methodological advantages in the spatial registration of data from the two modalities.

The primary objective of this study was to examine the association between hypoxia and vascular function in patients with treatment-naïve breast cancer using simultaneous ^{18}F-FMISO-PET/MRI. To our knowledge, this is the first such study in breast cancer.

Materials and methods

Study participants

Women aged >18 years with histologically-confirmed primary breast cancer and a tumour diameter >10 mm on mammography and/or ultrasound were eligible for the study (February 2017 to November 2018). Pregnancy, lactation, previous surgery or radiotherapy for cancer or benign breast disease, inadequate renal function and contraindications to MRI were exclusion criteria for the study. The research was approved by a National Research Ethics Committee (14/EE/0145). All study participants provided written informed consent before PET/MRI examination.

PET/MRI acquisition

Participants underwent a 60-min simultaneous PET/MR scan of the breasts in the prone position on a SIGNA PET/MR scanner (GE Healthcare), using a 16-channel bilateral breast array (RAPID Biomedical) 120 min (median [range]: 120.2 [119.8–127.5] min) after injection of 306 ± 14 MBq ^{18}F-FMISO. The uptake period post injection (p.i.) was used to enhance hypoxic-to-normoxic tissue-contrast and allow the free ^{18}F-FMISO concentrations in tissue and blood to reach equilibrium [25,26], a requirement for influx-rate constant (K_i) determination by Patlak analysis [27].

PET: Emission data from 120–180 min p.i. (12×5-min frames) were reconstructed using time-of-flight ordered-subsets expectation-maximization (TOF-OSEM) with 4 iterations and 28 subsets (Supplemental Methods I). Plasma radioactivity concentration from two venous blood samples, acquired immediately before and after PET/MR acquisition, was used to scale a ^{18}F-FMISO population-based arterial input function (AIF) derived from existing data, permitting calculation of K_i [28]; (Supplemental Methods II; Supplemental Figure 1; [29-31]).

MRI: The MRI protocol involved a 2-point Dixon sequence for PET attenuation correction, T_1 and T_2-weighted images, DWI, and a DCE series. Sequences were also acquired to measure B_1^+ transmission-field non-uniformity, using a Bloch-Siegert method, and baseline T_1 (T_{10}) as required for the pharmacokinetic analysis of DCE-MRI data [32]. DCE-MRI acquisition involved five pre-contrast images, followed by 43 phases after intravenous bolus injection of 0.1 mmol/kg of Gadovist (Bayer Healthcare). MRI sequence details are given in Supplemental Table 1.

Image analysis

Tumour regions were manually delineated in OsiriX, version 8.0.2 (Pixmeo SARL) by three radiologists in consensus (one, three and >20 years of experience in breast MRI). Regions were drawn on the peak-enhancing volumes of the DCE-MRI series on all contiguous axial sections encompassing the invasive part of tumour and including multifocal/multicentric disease (Supplemental Methods III). Synchronous bilateral cancers were regarded as independent lesions [34].

DCE-MRI: Pharmacokinetic analysis of the DCE-MRI series was performed in MIStar, version 3.2.63 (Apollo Medical Imaging) using the extended Tofts' model [35] to calculate: contrast influx-rate constant, K^{trans}; efflux-rate constant, k_{ep}; extravascular-extracellular volume fraction, v_e; and plasma volume fraction, v_p (Supplemental Methods III).

DWI: Calculation of apparent diffusion coefficient (ADC) maps was performed in OsiriX, using *b*-values of 0 and 900 s/mm^2. Mean lesion ADC was calculated by manually outlining whole tumour regions on the *b*=900 s/mm^2 image (Supplemental Methods III; [36]).

PET: Image frames from 150–180 min p.i. were averaged, rigidly registered to the peak-enhancing phase of the DCE-MRI series and subsequently employed for the determination of ^{18}F-FMISO uptake as mean and maximum standardised uptake values normalised by body-weight (SUV_{mean}, SUV_{max}), maximum tumour-to-plasma (T_{max}/P) and tumour-to-muscle

(T_{max}/M) ratios within the regions defined on the DCE-MRI. The influx rate of ^{18}F-FMISO into the trapped (hypoxic) tissue compartment (K_i) was determined by Patlak-plot analysis, utilising all frames in the registered ^{18}F-FMISO series and the scaled population-based AIF. Hypoxic fractions (%HF) in tumour regions were calculated as the percentage of voxels with K_i values >2×standard deviations (SD) of the mean K_i of normoxic muscle (Supplemental Methods III).

Histology

Histopathological information including tumour histological subtype, grade, oestrogen receptor (ER), progesterone receptor (PR) and human epidermal growth factor receptor-2 (HER2) status were obtained from core biopsies or surgical tumour specimens. Cancers with positive ER or PR expression were classified as hormone-receptor (HR) positive.

Statistics

Statistical analysis was performed in IBM SPSS Statistics for MacOS, v25.0 (IBM Corp.) or Matlab 2016b. Continuous data were assessed for normality using the Anderson-Darling test. Correlations between continuous variables were assessed using the Pearson correlation coefficient (r). t-tests were used for comparison between means of two groups, and ANOVA when more than two groups were compared. Where data were not normally distributed, or normality could not be assessed, Mann-Whitney U and Mood's median or Kruskal-Wallis H tests were employed for comparisons between two or more groups, respectively. p-values <0.05 were considered statistically significant.

Results

A total of 32 women were enrolled into the study. Two participants withdrew before the PET/MR examination. PET/MRI data and DCE-MRI data from two participants were excluded owing to inadequate acquisition of DCE-MRI and poor pharmacokinetic-model fitting respectively. In total, data from 29 participants with 32 biopsy-confirmed primary breast cancers were analysed. ADC calculations included data from 18 patients (19 lesions), who successfully completed the DWI examination.

Two-thirds of the lesions (21/32; 66%) were invasive ductal cancers (IDC). The majority of cancers (29/32; 91%) were either grade 2 or 3. HR-positive expression was noted for 31/32

(97%) lesions, with 24/32 (77%) cancers being HER2-negative. Tumour characteristics are summarised in Table 1. Additional clinical information is provided in Supplemental Table 2.

Relationship between ^{18}F-FMISO-PET and DCE-MRI parameters

Scatter plots indicating the relationships between DCE-MRI parameters and K_i or %HF are illustrated in Fig. 1. An inverse relationship was observed between mean lesion K_i and K^{trans}, v_e, and v_p (Fig. 1a-1d; Supplemental Figure 2 [36]), which was statistically significant for K_i *vs*. K^{trans} (r=-0.38, p=0.04), but not for K_i *vs*. v_e (r=-0.30, p=0.10) or v_p (r=-0.28, p=0.12). Associations between %HF and DCE-MRI parameters followed similar trends, also indicating a decrease in hypoxia with increasing K^{trans}, v_e, and v_p (Fig. 1e-1h). Statistically significant correlations were observed between %HF and both K^{trans} (r=-0.33, p=0.04) and v_e (r=-0.38, p=0.03). No correlation was observed between k_{ep} and either K_i (r=0.08, p=0.65) or %HF (r=0.02, p=0.90).

Fig. 2 presents axial slices through K_i and K^{trans} parametric maps of four tumours of different histological subtype, indicating heterogeneous spatial relationships between hypoxia and perfusion; other DCE-MRI parametric images are given in Supplemental Figure 3.

^{18}F-FMISO-PET and DCE-MRI parameters *vs*. tumour histology and grade

Hypoxic fractions >1% were observed in 6/32 (19%) cancers with an additional 8/32 (25%) lesions displaying hypoxic fractions greater than zero but less than 1%; the remaining 18/32 (56%) tumours had no measurable %HF. Dot plots of %HF *vs*. tumour histological subtype and grade are presented in Fig. 3. K_i, %HF and ^{18}F-FMISO uptake parameters showed no significant difference between different histological subtype or grade (Tables 2 and 3). Similarly, no significant differences were observed between histological groups or grades for the DCE-derived parameters (Tables 2 and 3), except for the efflux rate-constant k_{ep}, which displayed a statistically significant difference among grade 2 and 3 cancers (median [range]: 0.25 [0.13-0.34] *vs*. 0.30 [0.10-0.35] min^{-1}; p=0.01). Furthermore, analysis of hypoxia and K^{trans} values in the most vascularised area of the tumour (hotspot on DCE-MRI) yielded no significant differences among different subtypes or grades (Supplemental Tables 3 and 4).

Effect of tumour size on ^{18}F-FMISO-PET and DCE-MRI parameters

Table 4 presents correlations between imaging indices and tumour size as measured by longest diameter on MRI or pathological size. No or weak negative correlations were observed between tumour size and DCE-MRI parameters. Conversely, ^{18}F-FMISO-PET parameters correlated positively with size; %HF significantly correlated with pathological size (r=0.63, p=0.001), while ^{18}F-FMISO-PET uptake metrics displayed associations of moderate strength with longest diameter on MRI.

ADC *vs.* ^{18}F-FMISO-PET and DCE-MRI parameters

Positive correlations were observed between ADC and DCE-MRI indices (K^{trans}: r=0.24, p=0.34; v_e: r=0.29, p=0.25; v_p: r=0.20, p=0.43), except for k_{ep} which correlated negatively with ADC (r=-0.15, p=0.56; Figure 4); none of which were statistically significant. No correlations were observed between ADC and K_i or %HF (K_i: r=0.05, p=0.84; %HF r=0.04, p=0.88; Figure 5). Representative ADC maps are given in Fig. 6.

Discussion

This study explored the relationship between tumour hypoxia and vascular function in breast cancer using combined ^{18}F-FMISO-PET/MRI. Hypoxic fractions and K_i measured on ^{18}F-FMISO-PET showed inverse relationships with the DCE-MRI perfusion parameter K^{trans}, consistent with the generally accepted view that tumour hypoxia is a consequence of inadequate oxygen supply to the tumour [1]. Previous clinical studies in cervical and head-and-neck carcinomas have demonstrated significant negative correlations between contrast enhancement or pharmacokinetic parameters from DCE-MRI and polarographic pO_2 measurements or pimonidazole immunohistochemistry [37,38]. These findings are consistent with our results in breast cancer.

However, PET and DCE-MRI parametric images exhibited largely heterogeneous intra-tumoural patterns with hypoxic islands on K_i maps often colocalising with areas of increased K^{trans}. This spatially-discrepant relationship between hypoxia and perfusion has been previously documented, with the co-existence of hypoxic and hyperperfused tumour sub-volumes [39]. Various biological mechanisms, including hypoxia-induced angiogenesis, interstitial fluid pressure, a fluctuating haemodynamic response, increased oxygen diffusion distances from the microvasculature, and the presence of longitudinal oxygen gradients across tumour vessels have all been proposed to explain the occurrence of hypoxia in highly-perfused

areas [40,41]. Thus, although the general trend of our results would support the widely-accepted view that hypoxia develops in hypoperfused breast tumours, the diverse relationships observed in individual tumour sub-volumes indicate heterogeneity in hypoxia-perfusion patterns and reflect the variety of pathophysiological mechanisms occurring in cancers.

The weak relationship between PET hypoxia parameters with k_{ep} suggests that the degree of tumour hypoxia is more strongly influenced by vascular flow rather than vessel permeability. Li *et al* [42] have previously suggested that k_{ep} is a much more sensitive measure of vessel permeability than K^{trans}, as the latter represents a combined measure of blood flow, vessel permeability and capillary-surface area. Our findings broadly agree with previous research in cervical and head-and-neck carcinomas, which illustrated weaker correlations between hypoxia and permeability-surface-area product than between hypoxia and blood flow [37,43]. The relationship between K^{trans} and regional hypoxia observed in our study suggests this is due to fluctuations in tumour vascular flow rather than capillary permeability.

No or weak positive correlations were found between static ^{18}F-FMISO parameters (SUV_{mean}, SUV_{max}, T_{max}/M, T_{max}/P) and DCE-MRI metrics. In contrast, in human head-and-neck cancer, where hypoxia is often marked, ^{18}F-FMISO SUV measurements were negatively correlated with both K^{trans} and k_{ep} [20]. A plausible explanation for this disparity is the higher level of hypoxia typically encountered in head-and-neck cancer, which will lead to uptake values being more dominated by hypoxia-specific ^{18}F-FMISO trapping rather than non-specific tracer accumulation. Due to the higher contribution of non-specific ^{18}F-FMISO accumulation at low hypoxia levels [44], the use of uptake values in cancers without marked hypoxia may not accurately reveal relationships between hypoxia and perfusion.

No significant correlation was observed between PET hypoxia parameters and tumour grade or subtype. Our sample size of non-IDC cases was small for evaluating the impact of histology on tumour hypoxic status, but the presence of non-zero hypoxic fractions was observed in all histological subtypes studied. Hypoxic fractions and higher K_i were noted in both grade 2 and 3 tumours, and less so in grade 1 cancers. These findings are concordant with previously reported small differences in hypoxia between low and high-grade breast malignancy [2].

Correlations between DCE-MRI functional parameters and pathological size or MR tumour diameter yielded moderate negative relationships and conversely positive associations between ^{18}F-FMISO-PET hypoxia parameters and size. The size-related hypoxia changes could be

ascribed to diffusion-limited hypoxia, concomitant perfusion decreases or increased interstitial fluid pressure [45].

ADC has been shown to inversely correlate with cellular density [46], and therefore a reduction in ADC should theoretically be accompanied by an increase in tumour hypoxia. Our findings indicated no association between ADC and PET hypoxia parameters. This result could be explained by the molecular subtype of lesions in our sample, which predominantly consisted of ER-positive/HER2-negative cancers. Due to lower blood flow, ER-positive or HER2-negative lesions exhibit lower ADC values than ER-negative or HER2-positive cancers [47,48]. As ADC is affected not only by tissue cellularity but several pathophysiologic processes including blood flow, membrane permeability and the geometric architecture of the interstitial space [49,50], it is likely that the lack of association between the PET hypoxia parameters and ADC is a consequence of the combined effect of cellularity, perfusion and microvessel structure on ADC. This assertion is further supported by the weak correlations between DCE-MRI indices and ADC observed in this study. It should be noted however that inconsistent correlations between ADC and DCE-MRI parameters have been reported in tumours, including breast cancer [51-53].

We calculated hypoxic fractions based on a specific parameter for hypoxia namely influx rate-constant K_i. Despite the higher variability associated with kinetic parameter estimates, our choice was based on two considerations. First, several authors have reported lack of correlation between ^{18}F-FMISO uptake ratios and pO_2 measurements casting doubt on the accuracy of thresholds derived from static PET imaging for hypoxic quantification [54,55]. Kinetic parameters, including K_i, have provided superior correlations with physiological measures of hypoxia from pO_2 histography and immunohistochemistry [54,55]. Second, these thresholds have mostly been defined on measurements from head-and-neck cancers and are not necessarily applicable to other tumour types, including breast cancer.

The main limitations of our study are the small sample size and that the majority of cancers were HR-positive ductal carcinomas. Though our findings cannot be generalised to the full spectrum of histological/molecular subtypes encountered in breast cancer, our study indicates the presence of hypoxia in all histological subtypes studied independent of nuclear grade. While the majority of lesions (56%) examined were found to be non-hypoxic, it should be noted that breast tumours are generally less hypoxic than cancers of the head-and-neck, cervix

or lung and show greater variability in hypoxia among molecular subtypes, with basal-like subtypes being the most hypoxic [56].

Our demonstration of *in vivo* simultaneous measurement of perfusion and hypoxia is clinically important for three reasons. First, previous reports have indicated that tumours with a high hypoxia-perfusion ratio (i.e. hypoxia due to low perfusion) have a poorer prognosis and suboptimal treatment response [57,58]. In breast cancer, studies have described differences in the response to perfusion-related hypoxic exposure between molecular subtypes [59,60], emphasising the need for combined hypoxia-perfusion measurements to provide more accurate prognostic information or tailor treatment. Second, preoperative radiotherapy or radiochemotherapy regimes in early or locally advanced breast cancer have reported beneficial clinical outcomes [61,62]. Hypoxia and hypoperfusion are known to reduce the effectiveness of radiotherapy and chemotherapy, and the hypoxia-perfusion status of tumours at baseline could allow optimisation of these regimens. Third, tumour hypoxia can occur independently of hypoperfusion as evidenced in the oncology literature [39,40,57,58] and our findings. As such, the data presented here can be viewed as providing further indication of the benefit of non-invasive multi-modal assessment of the tumour microenvironment for disease characterisation.

In conclusion, we found a negative relationship between tumour hypoxia, measured by ^{18}F-FMISO-PET, and markers of perfusion and vascular function from DCE-MRI, endorsing the hypothesis of perfusion-driven hypoxia in breast cancer. No associations were observed between ^{18}F-FMISO-PET parameters and tumour histology or grade, but hypoxic fractions increased with lesion size. The intra-tumoural heterogeneity observed in hypoxia and perfusion images is consistent with the known complex relationship between perfusion and the hypoxic tumour micromilieu. The combined hypoxia-perfusion status of tumours may need to be considered in determining treatment efficacy or informing therapy selection in breast cancer, which could be achieved using simultaneous multi-modality imaging as reported here.

References

1. Vaupel P, Kallinowski F, Okunieff P (1989) Blood flow, oxygen and nutrient supply, and metabolic microenvironment of human tumors: a review. Cancer Res 49:6449-6465

2. Vaupel P, Schlenger K, Knoop C, Höckel M (1991) Oxygenation of human tumors: evaluation of tissue oxygen distribution in breast cancers by computerized O_2 tension measurements. Cancer Res 51:3316-3322

3. Hohenberger P, Felgner C, Haensch W, Schlag PM (1998) Tumor oxygenation correlates with molecular growth determinants in breast cancer. Breast Cancer Res Treat 48:97-106

4. Helczynska K, Kronblad A, Jögi A et al (2003) Hypoxia promotes a dedifferentiated phenotype in ductal breast carcinoma in situ. Cancer Res 63:1441-1444

5. Cooper C, Liu GY, Niu YL, Santos S, Murphy LC, Watson PH (2004) Intermittent hypoxia induces proteasome-dependent down-regulation of estrogen receptor α in human breast carcinoma. Clin Cancer Res 10:8720-8727

6. Semenza GL (2016) The hypoxic tumor microenvironment: A driving force for breast cancer progression. Biochim Biophys Acta 1863:382–391

7. Chia SK, Wykoff CC, Watson PH et al (2001) Prognostic significance of a novel hypoxia-regulated marker, carbonic anhydrase IX, in invasive breast carcinoma. J Clin Oncol 19:3660-3668

8. Generali D, Berruti A, Brizzi MP et al (2006) Hypoxia-inducible factor-1α expression predicts a poor response to primary chemoendocrine therapy and disease-free survival in primary human breast cancer. Clin Cancer Res 12:4562-4568

9. Dewhirst MW, Cao Y, Moeller B (2008) Cycling hypoxia and free radicals regulate angiogenesis and radiotherapy response. Nat Rev Cancer 8:425-437

10. Kimura H, Braun RD, Ong ET et al (1996) Fluctuations in red cell flux in tumor microvessels can lead to transient hypoxia and reoxygenation in tumor parenchyma. Cancer Res 56:5522-5228

11. Bristow RG, Hill RP (2008) Hypoxia and metabolism. Hypoxia, DNA repair and genetic instability. Nat Rev Cancer 8:180-192

12. Turnbull LW (2009) Dynamic contrast-enhanced MRI in the diagnosis and management of breast cancer. NMR Biomed 22:28-39

13. Partridge SC, Nissan N, Rahbar H, Kitsch AE, Sigmund EE (2017) Diffusion-weighted breast MRI: Clinical applications and emerging techniques. J Magn Reson Imaging 45:337-355

14. Krohn KA, Link JM, Mason RP (2008) Molecular imaging of hypoxia. J Nucl Med 49:129S-148S

15. Quintela-Fandino M, Lluch A, Manso L et al (2017) ^{18}F-fluoromisonidazole PET and activity of neoadjuvant nintedanib in early HER2-Negative breast cancer: A window-of-opportunity randomized trial. Clin Cancer Res 23:1432-1441

16. Ueda S, Saeki T, Osaki A, Yamane T, Kuji I (2017) Bevacizumab induces acute hypoxia and cancer progression in patients with refractory breast Cancer: multimodal functional imaging and multiplex cytokine analysis. Clin Cancer Res 23:5769-5778

17. Cheng J, Lei L, Xu J et al (2013) ^{18}F-fluoromisonidazole PET/CT: a potential tool for predicting primary endocrine therapy resistance in breast cancer. J Nucl Med 54:333-340

18. Asano A, Ueda S, Kuji I et al (2018) Intracellular hypoxia measured by ^{18}F-fluoromisonidazole positron emission tomography has prognostic impact in patients with estrogen receptor-positive breast cancer. Breast Cancer Res 20:78

19. Andrzejewski P, Wengert G, Helbich TH et al (2019) Sequential [^{18}F]FDG-[^{18}F]FMISO PET and multiparametric MRI at 3T for insights into breast cancer heterogeneity and correlation with patient outcomes: first clinical experience. Contrast Media Mol Imaging DOI: 10.1155/2019/1307247

20. Jansen JF, Schöder H, Lee NY et al (2010) Noninvasive assessment of tumor microenvironment using dynamic contrast-enhanced magnetic resonance imaging and ^{18}F-fluoromisonidazole positron emission tomography imaging in neck nodal metastases. Int J Radiat Oncol Biol Phys. 77:1403-1410

21. Gerstner ER, Zhang Z, Fink JR et al (2016) ACRIN 6684: Assessment of tumor hypoxia in newly diagnosed glioblastoma using ^{18}F-FMISO PET and MRI. Clin Cancer Res 22:5079-5086

22. Pinker K, Andrzejewski P, Baltzer P et al (2016) Multiparametric [^{18}F]Fluorodeoxyglucose/[^{18}F]Fluoromisonidazole positron emission tomography/ magnetic resonance imaging of locally advanced cervical cancer for the non-invasive detection of tumor heterogeneity: A pilot study. PLoS One 11:e0155333. DOI: 10.1371/journal.pone.0155333

23. Simoncic U, Leibfarth S, Welz S et al (2017) Comparison of DCE-MRI kinetic parameters and FMISO-PET uptake parameters in head and neck cancer patients. Med Phys 44:23582368

24. Taylor E, Zhou J, Lindsay P et al (2020) Quantifying reoxygenation in pancreatic cancer during stereotactic body radiotherapy. Sci Rep 10:1638

25. Rasey JS, Grunbaum Z, Magee S et al (1987) Characterization of radiolabeled fluoromisonidazole as a probe for hypoxic cells. Radiat Res 111:292–304

26. Muzi M, Peterson LM, O'Sullivan JN et al (2015) ^{18}F-fluoromisonidazole quantification of hypoxia in human cancer patients using image-derived blood surrogate tissue reference regions. J Nucl Med. 56:1223–1228.

27. Patlak CS, Blasberg RG, Fenstermacher JD (1983) Graphical evaluation of blood-to-brain transfer constants from multiple-time uptake data. J Cereb Blood Flow Metab 3:1-7

28. Belton M, Brilha S, Manavaki R et al (2016) Hypoxia and tissue destruction in pulmonary TB. Thorax 71:1145-1153

29. Koh WJ, Rasey JS, Evans ML et al (1992) Imaging of hypoxia in human tumors with [F-18]fluoromisonidazole. Int J Radiat Oncol Biol Phys 22:199-212

30. Rasey JS, Koh WJ, Evans ML, Peterson LM, Lewellen TK, Graham MM, Krohn KA (1996) Quantifying regional hypoxia in human tumors with positron emission tomography of [^{18}F]fluoromisonidazole: a pretherapy study of 37 patients. Int J Radiat Oncol Biol Phys 36:417-428

31. Bruehlmeier M, Roelcke U, Schubiger PA, Ametamey SM (2004) Assessment of hypoxia and perfusion in human brain tumors using PET with ^{18}F-fluoromisonidazole and ^{15}O-H_2O. J Nucl Med 45:1851-1859

32. Bedair R, Graves MJ, Patterson AJ et al (2016) Effect of radiofrequency transmit field correction on quantitative dynamic contrast-enhanced MR imaging of the breast at 3.0T. Radiology 279:368-377

33. Banelli B, Casciano I, Di Vinci A et al (2010) Pathological and molecular characteristics distinguishing contralateral metastatic from new primary breast cancer. Ann Oncol 21:1237-1242

34. Tofts PS, Brix G, Buckley DL et al (1999) Estimating kinetic parameters from dynamic contrast-enhanced T_1-weighted MRI of a diffusable tracer: standardized quantities and symbols. J Magn Reson Imaging 10:223-232

35. Baltzer P, Mann RM, Iima M et al (2020) Diffusion-weighted imaging of the breast-a consensus and mission statement from the EUSOBI International Breast Diffusion-Weighted Imaging working group. Eur Radiol 30:1436- 1450

36. Liney GP, Gibbs P, Hayes C, Leach MO, Turnbull LW (1999) Dynamic contrast-enhanced MRI in the differentiation of breast tumors: user-defined versus semi-automated region-of-interest analysis. J Magn Reson Imaging 10:945-949

37. Donaldson SB, Betts G, Bonington SC et al (2011) Perfusion estimated with rapid dynamic contrast-enhanced magnetic resonance imaging correlates inversely with vascular endothelial growth factor expression and pimonidazole staining in head-and-neck cancer: a pilot study. Int J Radiat Oncol Biol Phys 81:1176–1183

38. Cooper R, Carrington BM, Loncaster J et al (2000) Tumour oxygenation levels correlate with dynamic contrast-enhanced magnetic resonance imaging parameters in carcinoma of the cervix. Radiother Oncol 57:53–59

39. Grkovski M, Schöder H, Lee NY et al (2017) Multiparametric imaging of tumor hypoxia and perfusion with ^{18}F-fluoromisonidazole dynamic PET in head and neck cancer. J Nucl Med 58:1072-1080

40. Dewhirst MW, Navia IC, Brizel DM, Willett C, Secomb TW (2007) Multiple etiologies of tumor hypoxia require multifaceted solutions. Clin Cancer Res 13:375–377

41. Beaney RP, Lammertsma AA, Jones T, McKenzie CG, Halnan KE (1984) Positron emission tomography for in-vivo measurement of regional blood flow, oxygen utilisation, and blood volume in patients with breast carcinoma. Lancet 1(8369):131–134

42. Li SP, Padhani AR, Taylor NJ et al (2011) Vascular characterisation of triple negative breast carcinomas using dynamic MRI. Eur Radiol 21:1364–1373

43. Dickie BR, Rose CJ, Kershaw LE et al (2017) The prognostic value of dynamic contrast-enhanced MRI contrast agent transfer constant K^{trans} in cervical cancer is explained by plasma flow rather than vessel permeability. Br J Cancer 116:1436–1443

44. Nunn A, Linder K, Strauss HW (1995) Nitroimidazoles and imaging hypoxia. Eur J Nucl Med 22:265–280

45. Dadiani M, Margalit R, Sela N, Degani H (2004) High-resolution magnetic resonance imaging of disparities in the transcapillary transfer rates in orthotopically inoculated invasive breast tumors. Cancer Res 64:3155–3161

46. Surov A, Meyer HJ, Wienke A (2017) Correlation between apparent diffusion coefficient (ADC) and cellularity is different in several tumors: a meta-analysis. Oncotarget 8:59492- 59499

47. Jeh SK, Kim SH, Kim HS et al (2011) Correlation of the apparent diffusion coefficient value and dynamic magnetic resonance imaging findings with prognostic factors in invasive ductal carcinoma. J Magn Reason Imaging 3:102-109

48. Martincich L, Deantoni V, Bertotto I et al (2012) Correlations between diffusion-weighted imaging and breast cancer biomarkers. Eur Radiol 22:1519-1528

49. Le Bihan D (1995) Molecular diffusion, tissue microdynamics and microstructure. NMR Biomed 8:375-386

50. Le Bihan D (2013) Apparent diffusion coefficient and beyond: what diffusion MR imaging can tell us about tissue structure. Radiology 268:318-322

51. Chu JP, Mak HK, Yau KK, Zhang L, Tsang J, Chan Q, Ka-Kit Leung G (2012) Pilot study on evaluation of any correlation between MR perfusion (K^{trans}) and diffusion (apparent diffusion coefficient) parameters in brain tumors at 3 Tesla. Cancer Imaging 12:1-6

52. Arlinghaus LR, Li X, Rahman AR, Welch EB, Xu L, Gore JC, Yankeelov TE (2011) On the relationship between the apparent diffusion coefficient and extravascular extracellular volume fraction in human breast cancer. Magn Reson Imaging 29:630-638

53. Yankeelov TE, Lepage M, Chakravarthy A et al (2007) Integration of quantitative DCE-MRI and ADC mapping to monitor treatment response in human breast cancer: initial results. Magn Reson Imaging 25:1–13

54. Kelada OJ, Rockwell S, Zheng MQ et al (2017) Quantification of tumor hypoxic fractions using positron emission tomography with [^{18}F]Fluoromisonidazole ([^{18}F]FMISO) kinetic analysis and invasive oxygen measurements. Mol Imaging Biol 19:893–902

55. Shi K, Bayer C, Astner ST et al (2017) Quantitative analysis of [^{18}F]FMISO PET for tumor hypoxia: correlation of modeling results with immunohistochemistry. Mol Imaging Biol 19:120–129

56. Bhandari V, Hoey C, Liu LY et al (2019) Molecular landmarks of tumor hypoxia across cancer types. Nat Genet 51:308–318

57. Lehtiö K, Eskola O, Viljanen T et al (2004) Imaging perfusion and hypoxia with PET to predict radiotherapy response in head-and-neck cancer. Int J Radiat Oncol Biol Phys 59:971–982

58. Thorwarth D, Eschmann SM, Scheiderbauer J, Paulsen F, Alber M (2005) Kinetic analysis of dynamic ^{18}F-fluoromisonidazole PET correlates with radiation treatment outcome in head-and-neck cancer. BMC Cancer 5:152

59. Harrison H, Rogerson L, Gregson HJ, Brennan KR, Clarke RB, Landberg G (2013) Contrasting hypoxic effects on breast cancer stem cell hierarchy is dependent on ER-α status. Cancer Res 73:1420–1433

60. von Minckwitz G, Eidtmann H, Rezai M et al. (2012) Neoadjuvant chemotherapy and bevacizumab for HER2-negative breast cancer. N Engl J Med 366:299–309

61. Poleszczuk J, Luddy K, Chen L et al (2017) Neoadjuvant radiotherapy of early-stage breast cancer and long-term disease-free survival. Breast Cancer Res 19:75

62. Brackstone M, Palma D, Tuck AB et al (2017) Concurrent Neoadjuvant Chemotherapy and Radiation Therapy in Locally Advanced Breast Cancer. Int J Radiat Oncol Biol Phys 99:769–776

Table and Figure legends

Table 1: Clinical characteristics for the patient population (*n*=29).

Table 2: MRI and ^{18}F-FMISO-PET parameters with respect to tumour histology. Data are presented as median [range] or mean ± standard deviation (SD) as appropriate.

Table 3: MRI and ^{18}F-FMISO-PET parameters with respect to nuclear grade. Data are presented as median [range] or mean ± standard deviation (SD) as appropriate.

Table 4: Pearson correlation coefficient *r* (*p*-value) between tumour size, MRI and ^{18}F-FMISO-PET parameters.

Supplemental Table 1: MRI acquisition parameters.

Supplemental Table 2: Additional clinical data for the patient population (*n*=29).

Supplemental Table 3: Hotspot K^{trans} (mL/g/min) and ^{18}F-FMISO-PET parameters with respect to tumour histology. Data are presented as mean ± standard deviation (SD) or median [range] as appropriate.

Supplemental Table 4: Hotspot K^{trans} (mL/g/min) and ^{18}F-FMISO-PET parameters in the hotspot area with respect to nuclear grade. Data are presented as median [range] or mean ± standard deviation (SD) as appropriate.

Fig. 1: ^{18}F-FMISO-PET K_i and hypoxic fraction (%) *vs*. the following DCE-MRI parameters: (**a**,**e**) contrast influx rate, K^{trans} (mL/g/min); (**b**,**f**) contrast efflux rate, k_{ep} (min^{-1}); (**c**,**g**) fractional volume of extravascular-extracellular space, v_e; (**d**,**h**) plasma fractional volume, v_p. IDC: invasive ductal carcinoma; ILC: invasive lobular carcinoma; IMC: invasive mucinous carcinoma; Mixed: carcinoma of mixed ductal and lobular type.

Fig. 2: Axial images of four representative patients with: (**a**) invasive ductal carcinoma (IDC); (**b**) invasive lobular carcinoma (ILC); (**c**) invasive mucinous carcinoma (IMC); and (**d**) carcinoma of mixed ductal and lobular type (Mixed). (*Left-to-right*) DCE-MRI image at peak enhancement; K^{trans} map representing tumour perfusion for the lesion ROI overlaid on the peak enhancing DCE-MRI image; K_i map representing tumour hypoxia for the lesion ROI overlaid on the peak enhancing DCE-MRI image; scatter plot and regression line of K_i *vs*. K^{trans} voxel-values within the tumour. K^{trans}: contrast influx rate (mL/g/min); K_i: ^{18}F-FMISO influx rate (mL/cm^3/min); ADC: apparent diffusion coefficient (mm^2/s).

Fig. 3: Dot plots of hypoxic fraction (%) by (**a**) histological type and (**b**) nuclear grade.

Fig. 4: Apparent diffusion coefficient (ADC) *vs*. DCE-MRI parameters: (**a**) contrast influx rate, K^{trans}; (**b**) contrast efflux rate, k_{ep}; (**c**) fractional volume of extravascular-extracellular space, v_e; (**d**) plasma fractional volume, v_p. IDC: invasive ductal carcinoma; ILC: invasive lobular carcinoma; IMC: invasive mucinous carcinoma; Mixed: carcinoma of mixed ductal and lobular type.

Fig. 5: ^{18}F-FMISO-PET parameters *vs*. apparent diffusion coefficient (ADC): (**a**) influx rate K_i and (**b**) hypoxic fraction (%). IDC: invasive ductal carcinoma; ILC: invasive lobular carcinoma; IMC: invasive mucinous carcinoma; Mixed: carcinoma of mixed ductal and lobular type.

Fig. 6: Axial images of two patients with: (**a**) invasive ductal carcinoma (IDC); (**b**) invasive lobular carcinoma (ILC). (*Left-to-right*) DCE-MRI image at peak enhancement; K^{trans} map representing tumour perfusion for the lesion ROI overlaid on the peak enhancing DCE-MRI image; K_i map representing tumour hypoxia for the lesion ROI overlaid on the DCE-MRI image at peak enhancement; ADC map. K^{trans}: contrast influx rate (mL/g/min); K_i: ^{18}F-FMISO influx rate (mL/cm^3/min); ADC: apparent diffusion coefficient (mm^2/s).

Supplemental Figure 1: ^{18}F-FMISO population-based arterial input functions (AIFs) for four representative patients, each scaled by two venous plasma samples.

Supplemental Figure 2: Axial images of the four representative patients shown in Fig. 2 with: (**a**) invasive ductal carcinoma (IDC); (**b**) invasive lobular carcinoma (ILC); (**c**) invasive mucinous carcinoma (IMC); and (**d**) carcinoma of mixed ductal and lobular type (Mixed). (*Left to right*) DCE-MRI image at peak enhancement, K^{trans}, K_i, k_{ep}, v_e and v_p maps for the lesion ROI overlaid on the peak-enhancing DCE-MRI image. K^{trans}: contrast influx transfer rate (mL/g/min); k_{ep}: contrast efflux transfer rate (min^{-1}); v_e: fractional volume of extravascular-extracellular space; v_p: plasma fractional volume; K_i: ^{18}F-FMISO influx rate (mL/cm^3/min).

Supplemental Figure 3: Scatterplot and regression line of K_i (mL/cm^3/min) *vs*. K^{trans} (mL/g/min) in the most vascularised area of the tumour (hotspot). Hotspot K^{trans} was calculated by averaging pixel values within a 9-pixel square region placed around the area exhibiting the highest K^{trans} value on the K^{trans} parametric maps [36]. The region encompassing the hotspot K^{trans} area was subsequently superimposed on the corresponding co-registered K_i map to calculate the mean K_i values within the hotspot area. The Pearson correlation coefficient

between K_i and K^{trans} was r = -0.16 (p=0.40). K^{trans}: contrast influx rate; K_i: ^{18}F-FMISO influx rate.

Table 1: Clinical characteristics for the patient population (*n*=29).

Characteristic	***n* (%)**
Age at diagnosis (years)[a]	57 [37-78]
Lesions	32
Pathological size (mm)[a,b]	26 [10-142]
Lesion longest diameter on MRI	
≤20 mm	10 (31)
>20 mm	22 (69)
Histopathological subtype	
Ductal (IDC)	21 (66)
Lobular (ILC)	6 (19)
Mucinous (IMC)	2 (6)
Mixed[c]	3 (9)
Histological grade[d]	
1	3 (9)
2	16 (50)
3	13 (41)
Hormone-receptor status[e]	
Positive (ER or PR)	31 (97)
Negative	1 (3)
HER2 status[f]	
Positive	7 (22)
Negative	25 (78)

[a]Data presented as median [range].

[b]Pathological size measured on tumor specimens from patients undergoing primary surgery (*n*=21).

[c]Invasive carcinomas with presence of both lobular and ductal components on histology.

[d]Nottingham combined histologic grade.

[e]Tumors classified as ER or PR-positive, if >10% of the cells demonstrated nuclear staining by immunohistochemistry.

[f]Tumors classified as HER2-positive, if they scored 3+ on immunohistochemistry, or if they carried gene amplification as detected by fluorescence *in situ* hybridization (FISH).

ER: estrogen receptor; PR: progesterone receptor; HER2: human epidermal growth factor receptor 2.

Table 2: MRI and ^{18}F-FMISO-PET parameters with respect to tumour histology. Data are presented as median [range] or mean ± standard deviation (SD) as appropriate.

Parameter	Histology				*p*-value
	IDC	ILC	Mixed	IMC	
Lesions (*n*=31)	20	6	3	2	
K^{trans}	0.43 [0.14–1.97]	0.26 [0.10–0.94]	0.41 [0.23–0.45]	0.44 [0.25–0.64]	0.77[a]
k_{ep}	0.26 [0.10–0.35]	0.28 [0.17–0.35]	0.25 [0.19–0.25]	0.26 [0.25–0.26]	0.14[a]
v_e	0.46 [0.21–0.95]	0.39 [0.26–0.84]	0.44 [0.39–0.64]	0.49 [0.31–0.66]	0.30[a]
v_p	0.08 [0–0.55]	0.05 [0.01–0.2]	0.06 [0.03–0.19]	0.09 [0.06–0.13]	0.77[a]
Lesions (*n*=19)	14	3	1	1	
ADC ($\times 10^{-3}$)	0.90 [0.42–1.55]	1.05 [0.84–1.28]	1.02 [–]	2.46 [–]	0.51[b]
Lesions (*n*=32)	21	6	3	2	
K_i ($\times 10^{-3}$)	0.00 ± 0.52	0.37 ± 0.65	0.08 ± 0.61	0.97 ± 0.91	0.26[c]
%HF	0 [0–4.74]	0.10 [0–2.58]	0.13 [0–1.22]	1.54 [0–3.07]	0.63[a]
SUV_{max}	1.53 ± 0.41	1.77 ± 0.16	1.60 ± 0.21	1.25 ± 0.12	0.31[c]
SUV_{mean}	1.14 ± 0.26	1.27 ± 0.18	1.17 ± 0.16	1.07 ± 0.15	0.65[c]
T_{max}/M	1.02 ± 0.24	1.30 ± 0.29	1.09 ± 0.22	0.95 ± 0.02	0.12[c]
T_{max}/P	0.87 ± 0.22	0.83 ± 0.33	0.87 ± 0.09	0.84 ± 0.09	0.99[c]

[a]Mood's median test

[b]Mann-Whitney *U* test for malignancies of type IDC and ILC only (mixed and IMC lesions were not included in the comparison)

[c]One-way analysis of variance (ANOVA)

IDC: invasive ductal carcinoma; ILC: invasive lobular carcinoma; Mixed: invasive carcinoma with presence of lobular and ductal components; IMC: invasive mucinous carcinoma; K^{trans}: contrast influx rate (mL/g/min); k_{ep}: contrast efflux rate (min^{-1}); v_e: fractional volume of extravascular-extracellular space; v_p: plasma fractional volume; ADC: apparent diffusion coefficient (mm^2/s); K_i: ^{18}F-FMISO influx rate (mL/cm^3/min); %HF: percentage hypoxic fraction; SUV: standardised uptake value (g/mL); T_{max}/M: maximum tumour-to-muscle ratio; T_{max}/P: maximum tumour-to-plasma ratio.

Table 3

Table 3: MRI and ^{18}F-FMISO-PET parameters with respect to nuclear grade. Data are presented as median [range] or mean ± standard deviation (SD) as appropriate.

Parameter	Grade 1	Grade 2	Grade 3	*p*-value
Lesions (*n*=31)	3	15	13	
K^{trans}	0.41 [0.24-0.54]	0.24 [0.10-1.98]	0.45 [0.17-1.27]	0.29[a]
k_{ep}	0.29 [0.26-0.31]	0.25[*c] [0.13-0.34]	0.30[*d] [0.10-0.35]	0.009[**a]
v_e	0.38 [0.24-0.77]	0.45 [0.23-0.84]	0.43 [0.21-0.95]	0.65[a]
v_p	0.06 [0.05-0.08]	0.06 [0.00-0.55]	0.09 [0.00-0.37]	0.46[a]
Lesions (*n*=19)	1	9	9	
ADC ($\times 10^{-3}$)	1.08 [-]	1.05 [0.42-2.46]	0.84 [0.70-1.28]	0.34[b]
Lesions (*n*=32)	3	16	13	
K_i ($\times 10^{-3}$)	-0.18 ± 0.52	0.25 ± 0.58	0.06 ± 0.65	0.47[c]
%HF	0 [0-0.04]	0 [0-4.74]	0.04 [0-2.6]	0.35[a]
SUV_{max}	1.28 ± 0.29	1.55 ± 0.29	1.66 ± 0.46	0.28[c]
SUV_{mean}	0.98 ± 0.09	1.18 ± 0.19	1.18 ± 0.29	0.37[c]
T_{max}/M	0.96 ± 0.02	1.04 ± 0.17	1.56 ± 0.36	0.36[c]
T_{max}/P	0.78 ± 0.08	0.81 ± 0.20	0.85 ± 0.25	0.21[c]

[a]Kruskal-Wallis *H*

[b]Mann-Whitney *U* test for grade 1 and 2 cancers only (grade I lesions were not included in the comparison).

[c]One-way analysis of variance (ANOVA)

[d]Significant difference between grade 2 and 3 cancers (*p*=0.01). Pairwise multiple comparison analysis utilized the Dwass-Steel-Critchlow-Fligner method.

[*]$p<0.05$; [**]$p<0.01$

K^{trans}: contrast influx rate (mL/g/min); k_{ep}: contrast efflux rate (min^{-1}); v_e: fractional volume of extravascular-extracellular space; v_p: plasma fractional volume; ADC: apparent diffusion coefficient (mm^2/s); K_i: ^{18}F-FMISO influx rate (mL/cm^3/min); %HF: percentage hypoxic fraction (%); SUV: standardised uptake value (g/mL); T_{max}/M: maximum tumour-to-muscle ratio; T_{max}/P: maximum tumour-to-plasma ratio.

Table 4: Pearson correlation coefficient *r* (*p*-value) between tumour size, MRI and ^{18}F-FMISO-PET parameters.

Parameter	Tumour size (mm) Longest diameter on MRI	Pathological size
Lesions (*n*)	31	21
K^{trans}	-0.15 (0.42)	-0.16 (0.48)
k_{ep}	-0.04 (0.84)	-0.15 (0.48)
v_e	-0.04 (0.83)	-0.27 (0.22)
v_p	-0.13 (0.50)	-0.09 (0.70)
Lesions (*n*)	19	11
ADC ($\times 10^{-3}$)	0.06 (0.80)	0.56 (0.07)
Lesions (*n*)	32	21
K_i ($\times 10^{-3}$)	0.15 (0.29)	0.21 (0.48)
HF (%)	0.26 (0.16)	0.63 (0.001**)
SUV_{max}	0.48 (0.02*)	0.26 (0.24)
SUV_{mean}	0.42 (0.006**)	0.39 (0.07)
T_{max}/M	0.45 (0.01*)	0.32 (0.14)
T_{max}/P	0.43 (0.02*)	0.49 (0.02*)

$^{*}p<0.05$; $^{**}p<0.01$.

[a]Pathological size as measured on tumour specimens from patients undergoing primary surgery (*n*=21).

K^{trans}: contrast influx rate (mL/g/min); k_{ep}: contrast efflux rate (min^{-1}); v_e: fractional volume of extravascular-extracellular space; v_p: plasma fractional volume; ADC: apparent diffusion coefficient (mm^2/s); K_i: ^{18}F-FMISO influx rate (mL/cm^3/min); %HF: percentage hypoxic fraction; SUV: standardised uptake value (g/mL); T_{max}/M: maximum tumour-to-muscle ratio; T_{max}/P: maximum tumour-to-plasma ratio.

Figure 1

Click here to access/download;Figure;EuRa_Figure1_108x174mm_500x500.tif

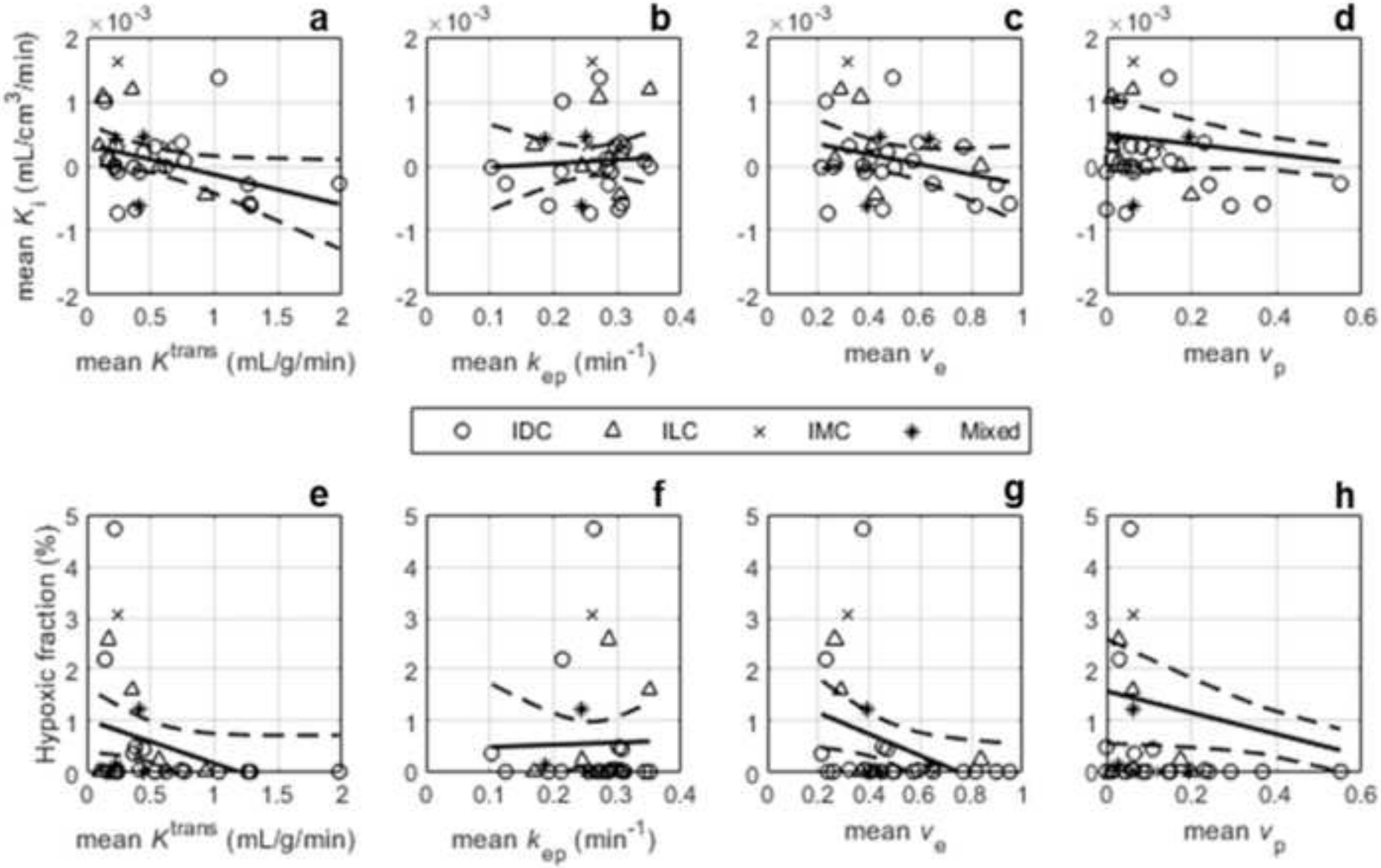

Figure 2

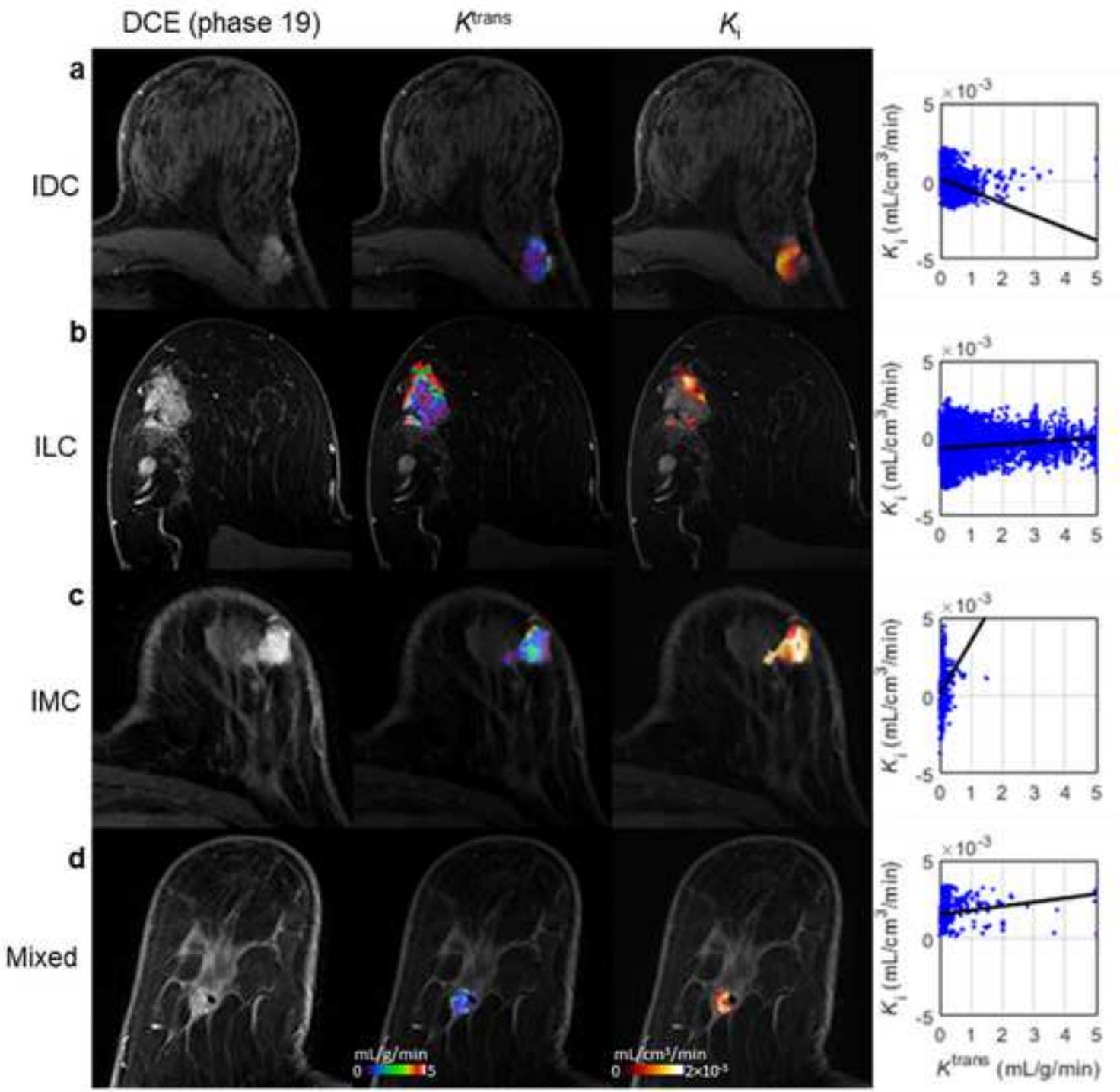

Figure 3

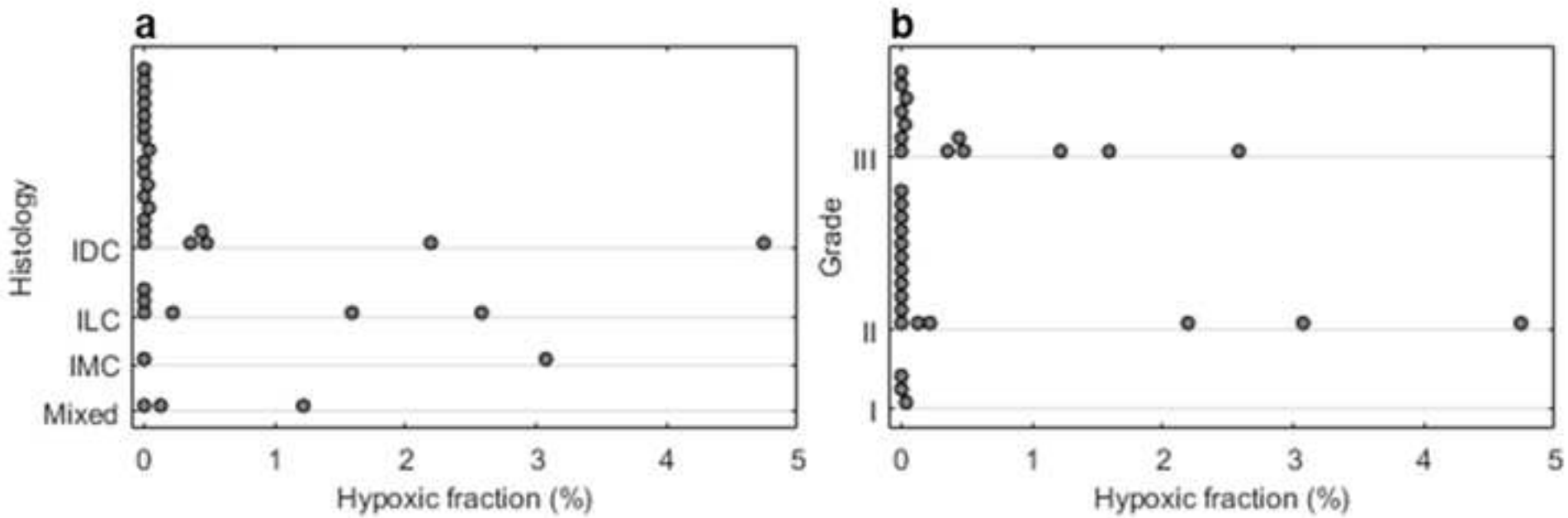

Figure 4

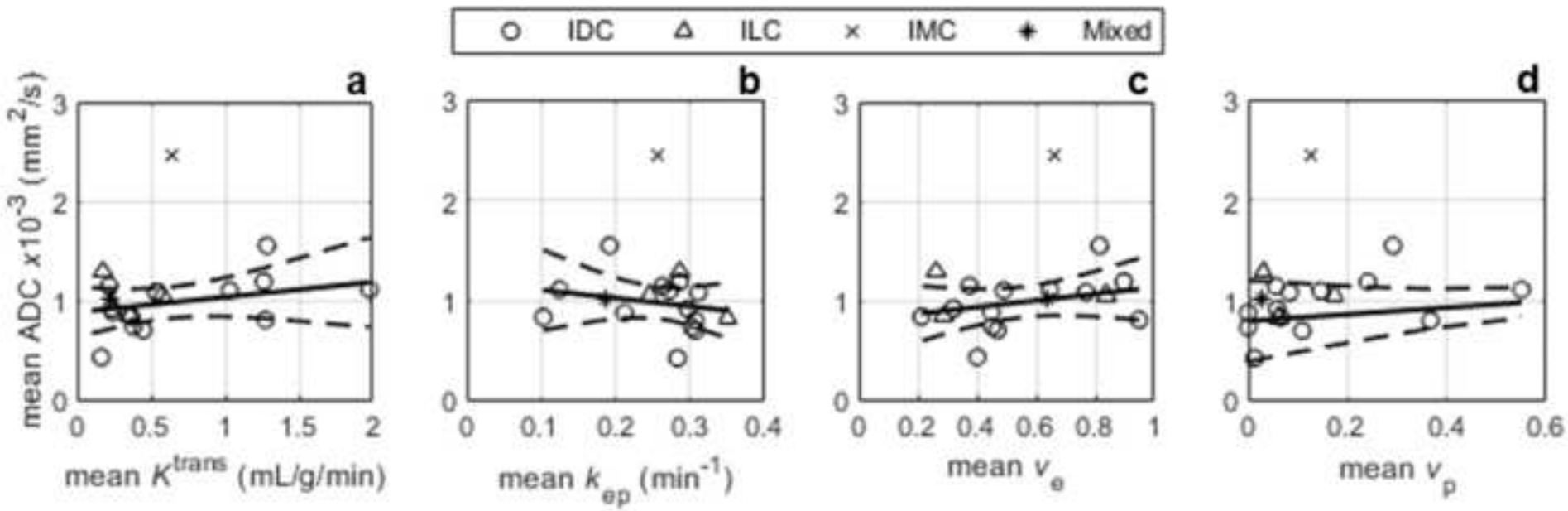

Figure 5

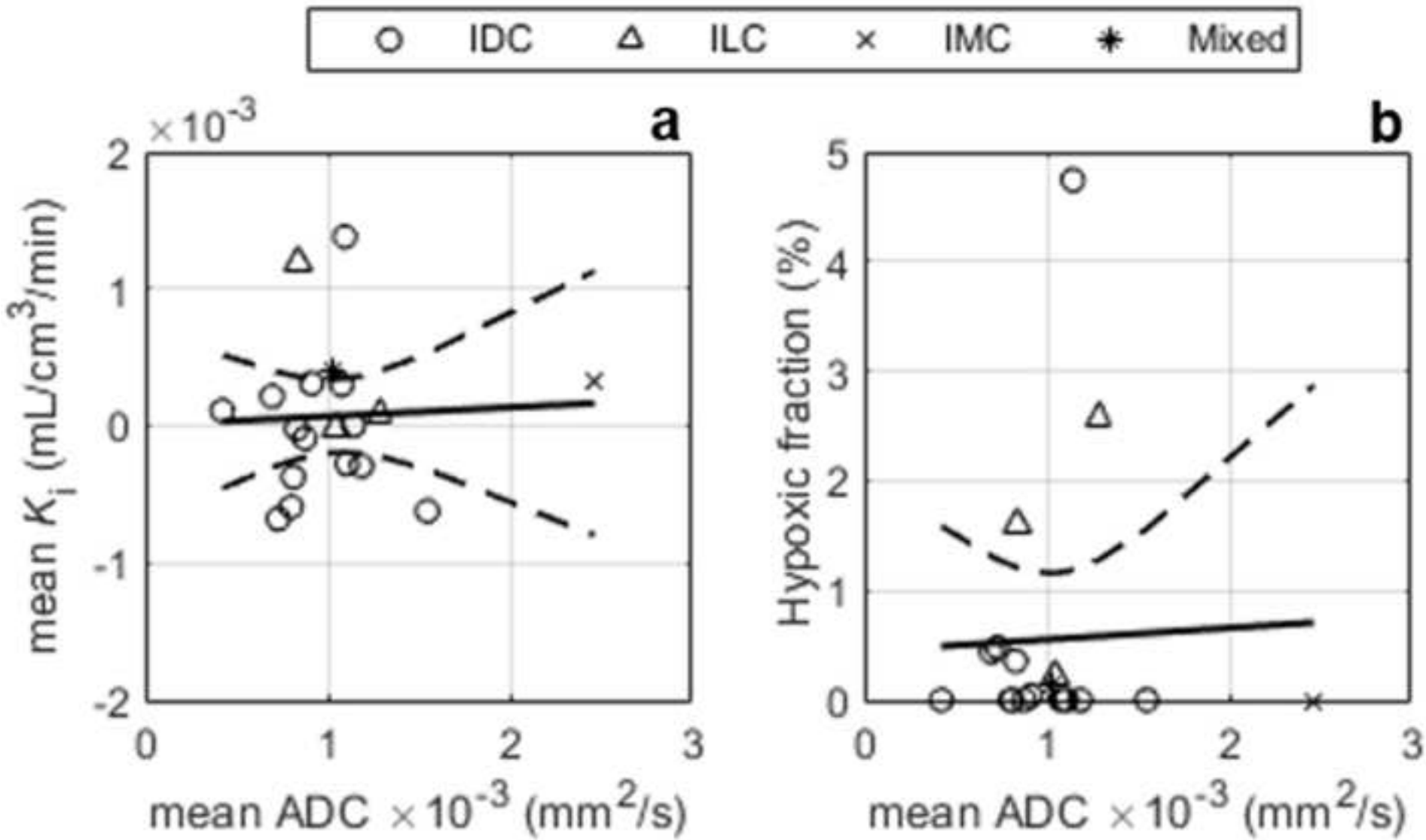

Figure 6

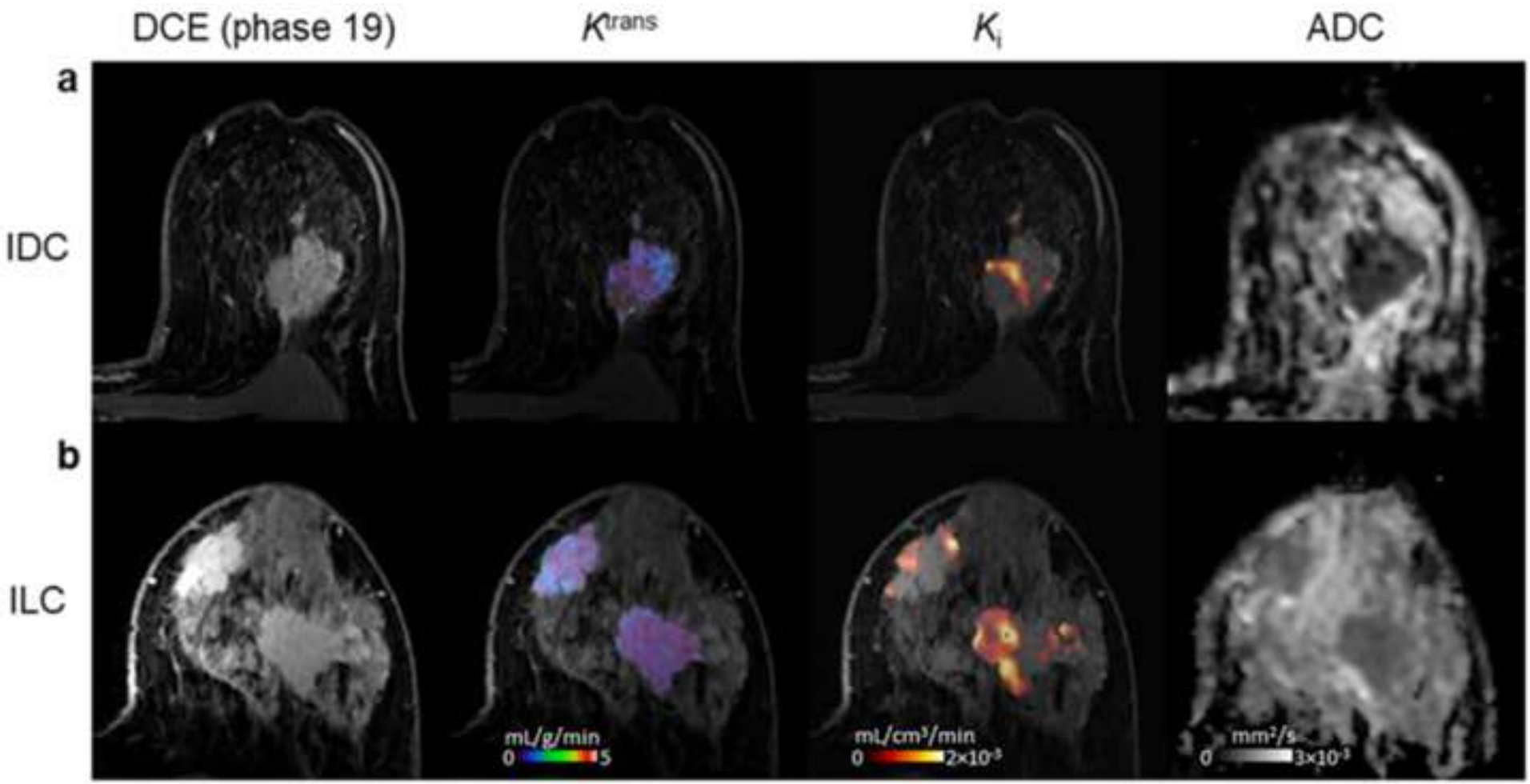

1. ***Acknowledgements***

The authors would like to thank the Radiopharmaceutical Unit, Wolfson Brain Imaging Centre, University of Cambridge for the provision of ^{18}F-FMISO; the radiographic team and research nurses at the Wolfson Brain Imaging Centre and the Department of Radiology, University of Cambridge, as well as the clinical staff at the Cambridge Breast Unit, Cambridge University Hospitals NHS Foundation Trust.

2. ***Funding***

This study was co-funded by Cancer Research UK (CRUK) – Cambridge Institute (CCCIT02) and the National Institute for Health Research (NIHR) Cambridge Biomedical Research Centre (BRC). J C Carmona-Bozo is supported by the Vargas Scholarship, Darwin College, University of Cambridge. R Manavaki, M J Graves and A J Patterson are supported by NIHR Cambridge BRC. F J Gilbert is a Senior Investigator at NIHR Cambridge BRC. The University of Cambridge PET/MR facility was funded by the Medical Research Council (MRC), UK. The views expressed are those of the authors and not necessarily those of the NIHR or the Department of Health and Social Care, UK.

Compliance with Ethical Standards

3. ***Guarantor:***

The scientific guarantor of this publication is Professor Fiona J Gilbert.

4. ***Conflict of Interest:***

The authors declare relationships with the following companies: FJG has research collaborations with Bayer Healthcare, GE Healthcare, Hologic Inc., and a consultancy arrangement with Google.

5. ***Statistics and Biometry:***

No complex statistical methods were necessary for this paper.

6. ***Informed Consent:***

Written informed consent was obtained from all subjects (patients) in this study.

7. ***Ethical Approval:***

Institutional Review Board approval was obtained. All procedures performed involving human participants were in accordance with the ethical standards of a National Research Ethics Committee (NRES Committee East of England – Cambridge Central; 14/EE/0145) and the Administration of Radioactive Substances Advisory Committee (ARSAC), UK.

8. Study subjects or cohorts overlap:

Study subjects or cohorts have not been previously reported.

9. Methodology

Methodology:

- prospective
- observational
- performed at one institution

Supplementary Material

Supplemental Methods

I. PET image reconstruction parameters

A 192×192×89 matrix with 3.12×3.12×2.78-mm voxels used for PET image reconstruction. Corrections for normalisation, dead-time, random events, scatter, attenuation, sensitivity and isotope decay were applied as implemented on the scanner, together with an isotropic 4-mm FWHM Gaussian post reconstruction filter.

II. Measurement of ^{18}F-FMISO radioactivity concentration in blood samples and scaling of the population-based arterial input function (AIF)

The ^{18}F-FMISO population-based arterial input function (AIF) used in this study was generated by averaging measured arterial input functions derived from six healthy volunteers scanned at the Wolfson Brain Imaging Centre, University of Cambridge as part of a study in stroke.

For each scan the ^{18}F-FMISO population-based AIF was scaled by two venous blood samples (~2 mL each) collected following arteriovenous equilibrium [29], prior to (107 ± 6.4 min) and after the end (186.9 ± 6.5 min) of the PET/MR acquisition. Immediately after collection, each blood sample was aliquoted into a sample tube and centrifuged (6000 rpm; 5 min) to separate plasma, of which ~0.5 mL was apportioned for measuring radioactivity using a Triathler gamma counter (HIDEX). The radioactivity concentration (Bq/mL) in each plasma sample was subsequently calculated accounting for radioisotope decay between the time of measurement and injection. Given the low levels of metabolism and protein binding of ^{18}F-FMISO in human plasma, no correction for ^{18}F-FMISO plasma metabolites or protein binding was performed [29-31]. To determine the scale factor applied to the ^{18}F-FMISO population-based AIF for each patient, the ratio between the measured ^{18}F-FMISO radioactivity concentration in each venous plasma sample and the population-derived AIF at the time of blood sampling was calculated and averaged across the two blood samples.

Example AIFs from four representative patients are illustrated in Supplemental Figure 1.

III. Image Analysis

Tumour region-of-interest delineation: Tumour regions-of-interest (ROIs) encompassed the enhancing tumour volume, while visually excluding normal breast parenchyma, fat, necrotic areas and large vessels. To guide region delineation on the DCE images, subtraction images were created in Osirix, version 8.0.2 (Pixmeo SARL), by subtracting pre-contrast images from the peak-enhancing phase of the DCE image series (~2 min from the start of enhancement). For the exclusion of large vessels, maximum-intensity projection (MIP) images were also generated from the subtraction image-set and used as an additional reference for ROI delineation.

For measurement of mean apparent diffusion coefficient (ADC) in lesions, whole tumour regions were demarcated on all axial slices encompassing the tumour on the b=900 s/mm^2 image, using the DCE post-contrast images as guidance, and subsequently propagated on the corresponding ADC map for each lesion. For ROI definition, care was taken to avoid tumour boundaries, non-enhancing lesion voxels, necrotic and cystic areas [36].

DCE-MRI: B_1^+-correction maps were generated from the Bloch-Siegert method using in-house software implemented in Matlab R2016b (Mathworks Inc.). T_{10} maps were computed in MIStar, version 3.2.63 (Apollo Medical Imaging) utilising the B_1^+-field maps to correct for spatial variations in flip angle. Prior to pharmacokinetic analysis, a cuboid region encompassing the tumour across the DCE-MRI series was motion corrected via a 3D affine model implemented in MIStar, utilising the peak-enhancing phase of the DCE image series as reference for co-registration. Modelling utilised the modified Fritz-Hansen AIF, with all parameters restricted to positive values [32].

DWI: ADC maps were calculated using the following equation:

$$\mathrm{ADC} = \frac{\ln\left(\frac{S_0}{S_1}\right)}{(b_1 - b_0)} \tag{1}$$

where S_0 and S_1 are the signal intensities in images obtained with b_0=0 s/mm^2 and b_1=900 s/mm^2.

PET: To reduce the impact of patient motion during acquisition, ^{18}F-FMISO dynamic image series were non-rigidly registered to the first frame using the Advanced Normalization Tools (ANTs) package (http://stnava.github.io/ANTs/). Registered frames from 150–180 min p.i. were averaged, rigidly registered to the peak-enhancing phase of the DCE-MRI series and subsequently employed for the determination of ^{18}F-FMISO uptake (SUV_{mean}, SUV_{max}, T_{max}/P, T_{max}/M) in the tumour regions defined on the DCE-MRI. The quality of the registrations was visually inspected by a breast radiologist. For T_{max}/M calculations, the mean radioactivity concentration in a bilateral region in the pectoral muscle was used to represent normoxic tissue. In two cases where lesions were located directly adjacent to pectoral muscle, regions were only placed in the contralateral muscle. Given that increased tracer uptake may represent high tracer delivery to a region rather than trapping under hypoxic conditions, the influx rate of ^{18}F-FMISO (K_i) into the trapped tissue compartment was determined as a more specific measure of tumour hypoxia. K_i maps were produced by Patlak-plot analysis, using in-house software implemented in Matlab R2016b. Image analysis was performed using Analyze 12.0 (AnalyzeDirect Inc.).

Supplemental Table 1: MRI acquisition parameters.

Acquisition parameters	T_1 mapping (VFA)	B_1^+ mapping (Bloch-Siegert)	DCE (VIBRANT-TRICKS)	DWI
Sequence	3D SPGR	2D SPGR	3D SPGR	2D SE-EPI
Acquisition plane	Axial	Axial	Axial	Axial
FOV diameter (mm)	350	350	350	360
Image matrix	256×256	128×128	512×512	140×192
Slice thickness (mm)	2.8	7.0	2.8 (interpolated to 1.4)	4.0
No. of slices	112	22	112	26
b-values (s/mm^2)	n/a	n/a	n/a	0, 900
Pixel size (mm)	1.4×1.4	2.7×2.7	0.6×0.6	2.6×1.9
Fat suppression	No	No	Yes[a]	Yes[a]
ASSET factor	2	n/a	2.5	2
TR (ms)	4.2	24	7.1	6.0
TE (ms)	2.1	13.7	3.8	94.9
RF excitation (degrees)	2, 3, 5, 10, 15	20	12	90
No. of averages	1	1	0.5	5
Bandwidth (kHz)	62.5	15.6	125	250
Acquisition time	33 s (per flip angle)	2 m 20 s	8 m 5 s[b]	10 m 48 s

[a]Spatial-spectral water excitation

[b]Nominal temporal resolution: 10 s per phase

VFA: variable flip angle; VIBRANT-TRICKS: volume image breast assessment–time-resolved imaging of contrast kinetics; 3D SPGR: three-dimensional spoiled gradient recalled echo; 2D SPGR: two-dimensional spoiled gradient recalled echo; 2D SE-EPI: two-dimensional spin echo–echo-planar imaging; FOV: field-of-view; ASSET: array spatial sensitivity encoding technique.

Table 2: DCE-MRI and ^{18}F-FMISO-PET parameters with respect to tumor histology. Data are presented as median [range] or mean ± standard deviation (SD) as appropriate.

Parameter	Histology				*p*-value
	IDC	ILC	Mixed	IMC	
Lesions (*n*=31)	20	6	3	2	
K^{trans}	0.43 [0.14–1.97]	0.26 [0.10–0.94]	0.41 [0.23–0.45]	0.44 [0.25–0.64]	0.77[a]
k_{ep}	0.26 [0.10–0.35]	0.28 [0.17–0.35]	0.25 [0.19–0.25]	0.26 [0.25–0.26]	0.14[a]
v_e	0.46 [0.21–0.95]	0.39 [0.26–0.84]	0.44 [0.39–0.64]	0.49 [0.31–0.66]	0.30[a]
v_p	0.08 [0–0.55]	0.05 [0.01–0.2]	0.06 [0.03–0.19]	0.09 [0.06–0.13]	0.77[a]
Lesions (*n*=32)	21	6	3	2	
K_i ($\times 10^{-3}$)	0.00 ± 0.52	0.37 ± 0.65	0.08 ± 0.61	0.97 ± 0.91	0.26[b]
%HF	0 [0–4.74]	0.10 [0–2.58]	0.13 [0–1.22]	1.54 [0–3.07]	0.63[a]
SUV_{max}	1.53 ± 0.41	1.77 ± 0.16	1.60 ± 0.21	1.25 ± 0.12	0.31[b]
SUV_{mean}	1.14 ± 0.26	1.27 ± 0.18	1.17 ± 0.16	1.07 ± 0.15	0.65[b]
T_{max}/M	1.02 ± 0.24	1.30 ± 0.29	1.09 ± 0.22	0.95 ± 0.02	0.12[b]
T_{max}/P	0.87 ± 0.22	0.83 ± 0.33	0.87 ± 0.09	0.84 ± 0.09	0.99[b]

[a]Mood's median test

[c]One-way analysis of variance (ANOVA)

IDC: invasive ductal carcinoma; ILC: invasive lobular carcinoma; Mixed: invasive carcinoma with presence of lobular and ductal components; IMC: invasive mucinous carcinoma; K^{trans}: contrast influx rate (mL/g/min); k_{ep}: contrast efflux rate (min^{-1}); v_e: fractional volume of extravascular-extracellular space; v_p: plasma fractional volume; K_i: ^{18}F-FMISO influx rate (mL/cm^3/min); %HF: percentage hypoxic fraction; SUV: standardized uptake value (g/mL); T_{max}/M: maximum tumor-to-muscle ratio; T_{max}/P: maximum tumor-to-plasma ratio.

Table 3: DCE-MRI and ^{18}F-FMISO-PET parameters with respect to nuclear grade. Data are presented as median [range] or mean ± standard deviation (SD) as appropriate.

Parameter	Grade 1	Grade 2	Grade 3	*p*-value
Lesions (*n*)	3	15	13	
K^{trans}	0.41 [0.24-0.54]	0.24 [0.10-1.98]	0.45 [0.17-1.27]	0.29[a]
k_{ep}	0.29 [0.26-0.31]	0.25[*c] [0.13-0.34]	0.30[*c] [0.10-0.35]	0.009[**a]
v_e	0.38 [0.24-0.77]	0.45 [0.23-0.84]	0.43 [0.21-0.95]	0.65[a]
v_p	0.06 [0.05-0.08]	0.06 [0.00-0.55]	0.09 [0.00-0.37]	0.46[a]
Lesions (*n*)	3	16	13	
K_i ($\times 10^{-3}$)	-0.18 ± 0.52	0.25 ± 0.58	0.06 ± 0.65	0.47[b]
%HF	0 [0-0.04]	0 [0-4.74]	0.04 [0-2.6]	0.35[a]
SUV_{max}	1.28 ± 0.29	1.55 ± 0.29	1.66 ± 0.46	0.28[b]
SUV_{mean}	0.98 ± 0.09	1.18 ± 0.19	1.18 ± 0.29	0.37[b]
T_{max}/M	0.96 ± 0.02	1.04 ± 0.17	1.56 ± 0.36	0.36[b]
T_{max}/P	0.78 ± 0.08	0.81 ± 0.20	0.85 ± 0.25	0.21[b]

[a]Kruskal-Wallis *H*

[b]One-way analysis of variance (ANOVA)

[c]Significant difference between grade 2 and 3 cancers (p=0.01). Pairwise multiple comparison analysis utilized the Dwass-Steel-Critchlow-Fligner method.

$^{*}p<0.05$; $^{**}p<0.01$

K^{trans}: contrast influx rate (mL/g/min); k_{ep}: contrast efflux rate (min^{-1}); v_e: fractional volume of extravascular-extracellular space; v_p: plasma fractional volume; K_i: ^{18}F-FMISO influx rate (mL/cm^3/min); %HF: percentage hypoxic fraction (%); SUV: standardized uptake value (g/mL); T_{max}/M: maximum tumor-to-muscle ratio; T_{max}/P: maximum tumor-to-plasma ratio.

Table 4: Pearson correlation coefficient *r* (*p*-value) between tumor size and DCE-MRI and ^{18}F-FMISO-PET parameters.

Parameter	Tumor size (mm) Longest diameter on MRI	Pathological size
Lesions (*n*)	31	21
K^{trans}	-0.15 (0.42)	-0.16 (0.48)
k_{ep}	-0.04 (0.84)	-0.15 (0.48)
v_e	-0.04 (0.83)	-0.27 (0.22)
v_p	-0.13 (0.50)	-0.09 (0.70)
Lesions (*n*)	32	21
K_i ($\times 10^{-3}$)	0.15 (0.29)	0.21 (0.48)
HF (%)	0.26 (0.16)	0.63 (0.001**)
SUV_{max}	0.48 (0.02*)	0.26 (0.24)
SUV_{mean}	0.42 (0.006**)	0.39 (0.07*)
T_{max}/M	0.45 (0.01*)	0.32 (0.14)
T_{max}/P	0.43 (0.02*)	0.49 (0.02*)

$^{*}p<0.05$; $^{**}p<0.01$.

K^{trans}: contrast influx rate (mL/g/min); k_{ep}: contrast efflux rate (min^{-1}); v_e: fractional volume of extravascular-extracellular space; v_p: plasma fractional volume; K_i: ^{18}F-FMISO influx rate (mL/cm^3/min); %HF: percentage hypoxic fraction; SUV: standardized uptake value (g/mL); T_{max}/M: maximum tumor-to-muscle ratio; T_{max}/P: maximum tumor-to-plasma ratio.

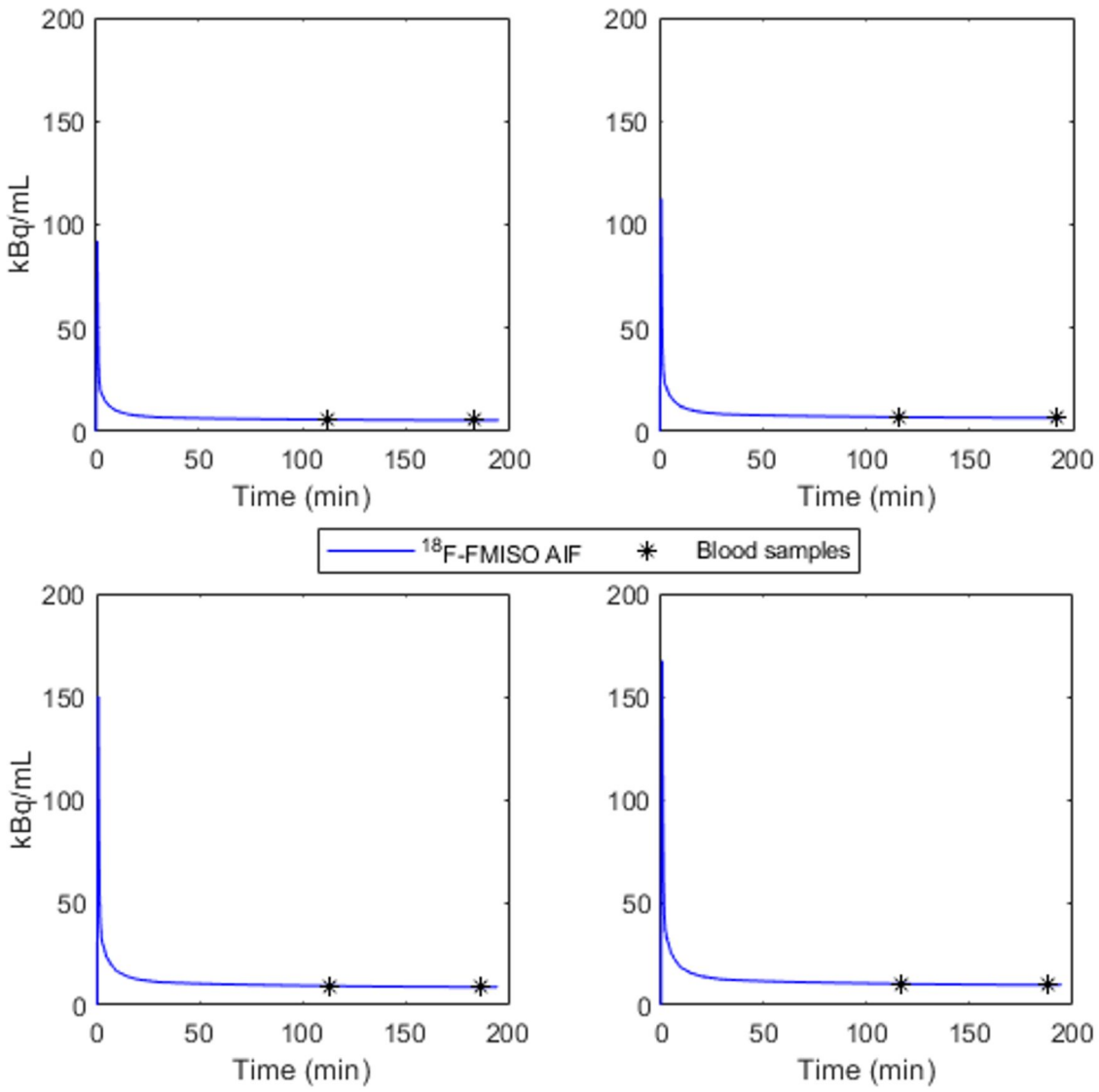
kBq/mL
Time (min)
0
50
100
150
200
^{18}F-FMISO AIF
Blood samples

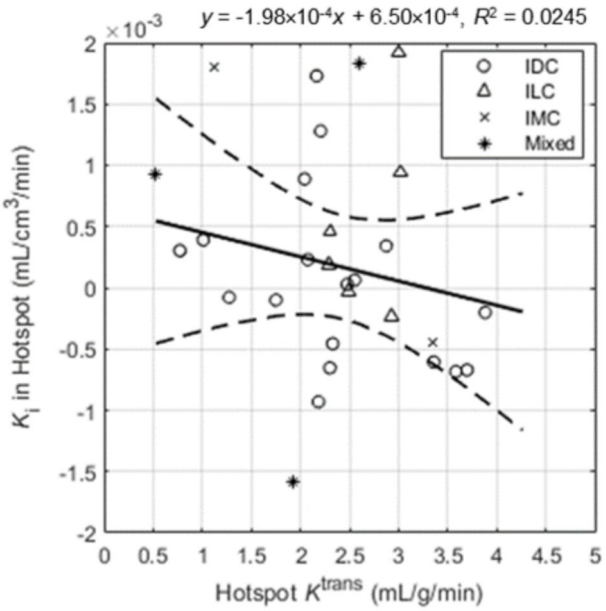
y = -1.98×10-4x + 6.50×10-4, R2 = 0.0245
×10-3
2
1.5
1
0.5
0
-0.5
-1
-1.5
-2
0
0.5
1
1.5
2
2.5
3
3.5
4
4.5
5
IDC
ILC
IMC
Mixed
Ki in Hotspot (mL/cm3/min)
Hotspot Ktrans (mL/g/min)

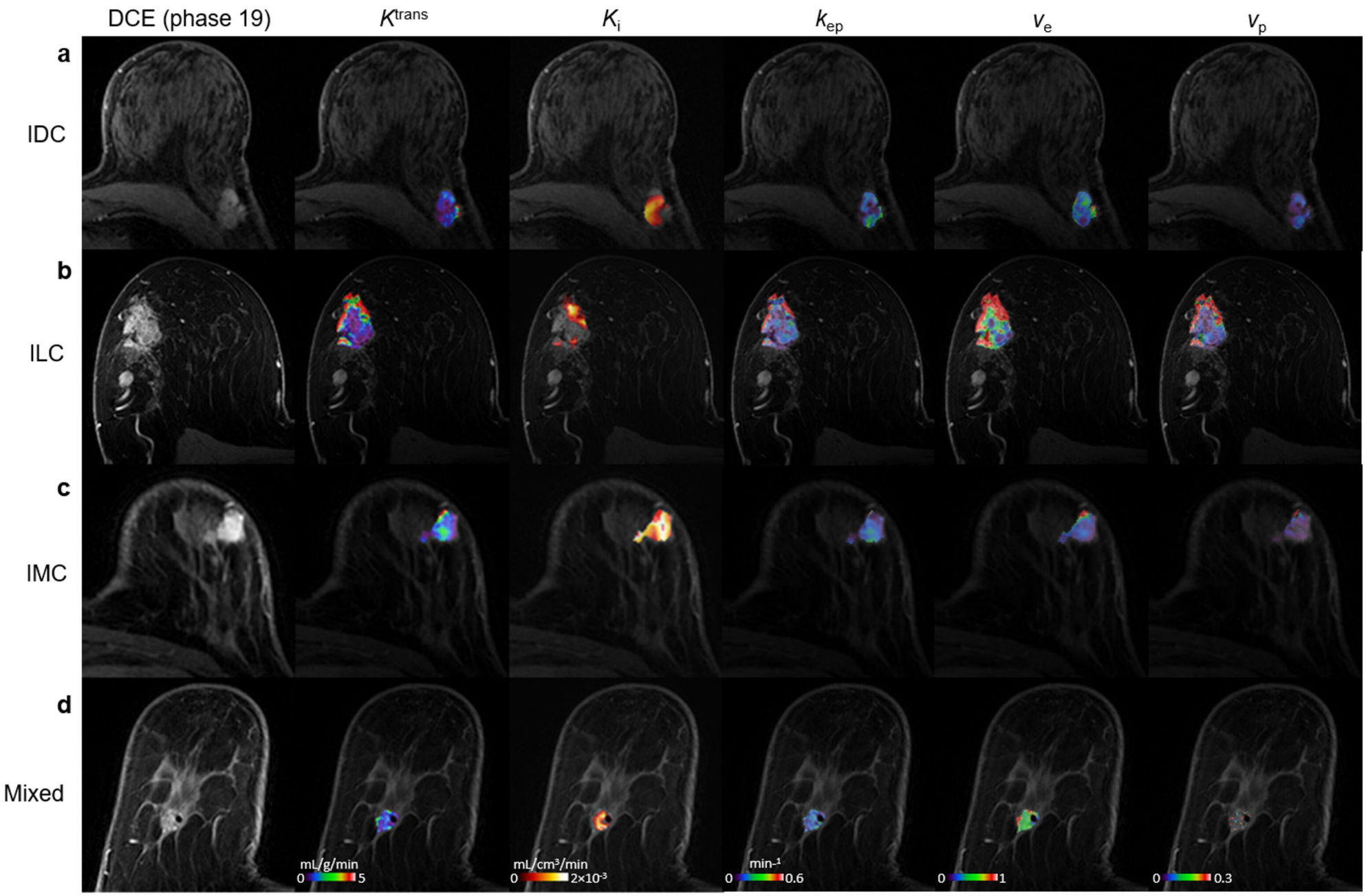
DCE (phase 19)
K^{trans}
K_i
k_{ep}
v_e
v_p
a
IDC
b
ILC
c
IMC
d
Mixed
mL/g/min
0
5
mL/cm³/min
0
2×10⁻³
min⁻¹
0
0.6
0
1
0
0.3